A. Montorfano, F. Piscaglia, M. Schmitt, Y.M. Wright, C.E. Frouzakis, A.G. Tomboulides, K. Boulouchos, A. Onorati
Comparison of Direct and Large Eddy Simulations of the Turbulent Flow in a Valve/piston Assembly
Flow, Turbulence and Combustion, Vol. 95, N. 2-3, 2015, p. 461-480
doi:10.1007/s10494-015-9620-6

FTC manuscript No.
(will be inserted by the editor)

Comparison of Direct and Large Eddy Simulations of the Turbulent Flow in a Valve/Piston Assembly

Andrea Montorfano · Federico Piscaglia · Martin Schmitt · Yuri M. Wright · Christos E. Frouzakis · Ananias G. Tomboulides · Konstantinos Boulouchos · Angelo Onorati

Received: date / Accepted: date

Abstract The dynamics and evolution of the turbulent flow inside an experimentally investigated engine-like geometry consisting of a flat-top cylinder head with a fixed, axis-centered valve and low-speed piston were studied numerically by means of Direct Numerical Simulation (DNS) and Large Eddy Simulation (LES), with a particular focus on Cycle-to-Cycle Variability (CCV). DNS was performed by the spectral element code nek5000 on a 58M points grid, whereas LES was carried out by the finite volume software OpenFOAM on a 4.6M hexahedral mesh. Results obtained by DNS and LES are compared with respect to the velocity means and fluctuations, as well with other derived quantities, achieving good agreement between simulations and experiments. The cyclic variability and complex unsteady flow features like the laminar-to-turbulent transition and the evolution of the tumble vortices were studied by time-resolved analysis and Proper Orthogonal Decomposition (POD). Simulations show that during the first half of the intake stroke the flow field is dominated by the dynamics of the incoming jet and the vortex rings it creates. With decreasing piston speed, the large central ring becomes the dominant flow feature until the top dead center. The flow field at the end of the previous cycle is found to have a strong effect on the jet breakup process and the dynamics of the vortex ring below the valve of the subsequent cycle as well as on the observed significant cyclic variations.

Keywords Large Eddy Simulation · Direct Numerical Simulation · engine-like geometry · Cyclic Variability · Proper Orthogonal Decomposition · turbulence modeling

1 Introduction

Among all physical phenomena that occur inside the cylinder of an internal combustion engine (ICE), turbulence certainly has a direct impact on thermodynamic efficiency, brake

Andrea Montorfano (✉) E-mail: andrea.montorfano@polimi.it, ph. +39 02 2399 3804
Federico Piscaglia, Angelo Onorati
Energy Department, Politecnico di Milano, Milano, Italy.

Martin Schmitt, Yuri M. Wright, Christos E. Frouzakis, Konstantinos Boulouchos
Aerothermochemistry and Combustion System Laboratory, ETH Zurich, Switzerland

Ananias G. Tomboulides
Department of Mechanical Engineering, University of Western Macedonia, Greece

power and emissions of the engine since its influence extends from volumetric efficiency to air/fuel mixing, combustion and heat transfer. Historically, turbulent flows have been simulated mainly by models based on Reynolds averaging of the Navier-Stokes equations (RANS), either in their original version or in the unsteady (URANS) formulation for slowly varying flows [24]. URANS approaches have proved to yield very good predictions of phase-averaged flow fields, including macroscopic features of the charge motion like the swirl and tumble vortices [1]. On the other hand, most of the time-varying quantities characterizing in-cylinder flows cannot be resolved by models based on implicit time- or ensemble-averaging methods like URANS: small-scale turbulence, cycle-to-cycle variability (CCV) and in-cycle evolution of three-dimensional structures (jets and vortices) can be simulated only by a time-resolved (rather than time-averaged) approach like Large Eddy Simulation (LES) [26] or Direct Numerical Simulation (DNS). In recent years, LES has been successfully applied to ICE simulation by several authors, including Haworth *et al.* [10,11], Thobois *et al.* [32,33], and Hasse *et al.* [9], showing that good predictions of mean and fluctuating velocity together with estimation of turbulence-driven CCV can be obtained by LES. Nevertheless, due to its lack of closure models for turbulence, DNS can be regarded as the main tool to carry out fundamental studies of unsteady flows.

The aim of this paper is to further explore the potential of LES and DNS for ICE simulation. A simplified engine-like geometry for which experimental data are available [16] was simulated by both LES [15] and DNS [27], and validation of flow statistics (average velocity and Reynolds stresses) was carried out to assess the capability of each approach to predict the basic flow features. The dynamics of in-cylinder turbulence was investigated, with particular focus on the evolution of the vortex structures during multiple engine cycles and the possible causes of turbulence-driven Cycle-to-Cycle Variability (CCV). LES results were further post-processed by means of Proper Orthogonal Decomposition (POD) to evaluate the potential of this tool in the analysis of dynamic systems like the present one.

DNS simulations were carried out by the spectral element solver nek5000 [6], while the finite volume open-source software OpenFOAM® [31] was applied for LES. In particular, the DNS code was was extended with an arbitrary Lagrangian/Eulerian approach (ALE) to account for moving grids, while specific sub-models for LES were implemented by the authors in the OpenFOAM® technology [18–20,23] and were used in the present work; modifications included the implementation of a compressible WALE subgrid-scale model [17], improvements to the mesh motion strategy [21,22,14] and appropriate boundary and initial conditions for LES which includes turbulent structures (generated artificially at the boundary), with physically sound spatial and temporal correlations [13]. Algorithms for data post-processing methods like the Proper Orthogonal Decomposition (POD) have also been implemented [15].

The paper is organized as follows: the presentation of the simulated geometry and the numerical setup is followed by the validation of the LES approach by comparison against experimental and DNS data. Finally, a more detailed analysis of dynamic flow features is presented and the results are discussed.

2 Geometry and case description

The 3-D geometry of the valve/piston assembly (Fig. 1), which was investigated experimentally by Morse *et al.* [16] using Laser Doppler Anemometry, has a diameter of $D = 75$ mm, a stroke of $S = 60$ mm and the piston moves with a turning speed of $n = 200$ rpm. The clearance c, i.e. the distance between piston and cylinder head at TDC, is 30 mm. A large plenum

(not shown) upstream of the valve was employed to avoid specifying boundary conditions at the valve gap. The valve is coaxial with respect to the cylinder and remains fixed throughout

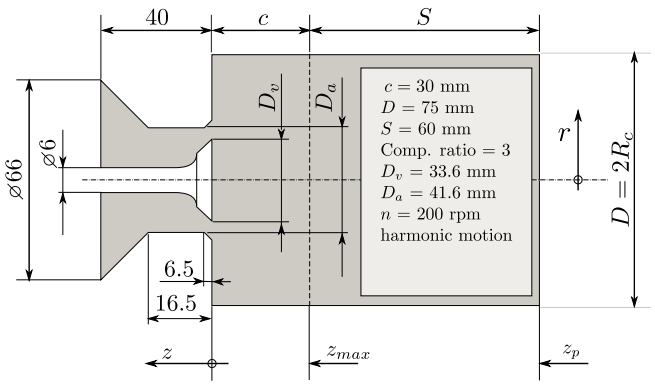

Fig. 1 Geometry of the valve/piston assembly. The large upstream plenum connected to the intake section is not shown.

the whole engine cycle, so it does not open nor close. Piston motion is purely sinusoidal, with a period of 360 Crank-Angle (CA) degrees. Due to the low piston velocity, the flow regime in the valve seat during the intake stroke is laminar. A circular jet is expected to form in the cylinder during this phase, together with primary and secondary vortex rings as a consequence of the interaction of the incoming flow with the fluid inside the cylinder. The maximum flow Mach number remains well below 0.3 for all crank-angle positions, therefore the flow dynamics could be approximated by the incompressible Navier-Stokes equations. Nevertheless, the LES solver was developed by taking into account possible density variations within the flow. The rationale for this (apparently unneeded) choice was to obtain a validation of the compressible solver also, that is currently used for the simulation of real engine configurations where compressibility effects (due, e.g., to high compression ratios, heat transfer, combustion, etc.) are indeed relevant.

3 Numerical methodology

3.1 Direct Numerical Simulation

In order to account for the mesh variation resulting from the piston movement, the highly scalable spectral element solver nek5000 [6] was extended with an Arbitrary Lagrangian/Eulerian (ALE) approach for the so-called $P_N - P_N$ formulation where pressure and velocity are solved on the same grid [27]. The Navier-Stokes equations are integrated using a 3rd-order semi-implicit scheme treating the non-linear advection term explicitly while the viscous term is accommodated by an implicit third-order backward differentiation scheme. No discretization is required to update the mesh velocity, since it is a-priori specified by the piston kinematics.

For the spatial discretization the computational domain is split into conforming curve-sided hexahedral elements and the solution and geometry are expressed in terms of 7-th order Lagrange polynomials which are based on Gauss-Lobatto-Legendre quadrature points

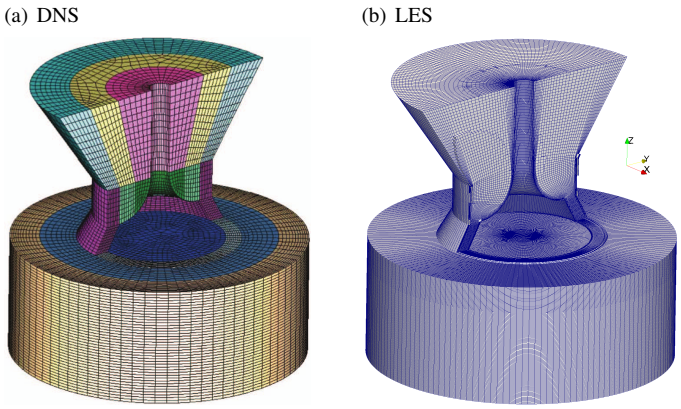

Fig. 2 (a) Spectral element skeleton used for DNS; (b) Finite Volume mesh used for LES.

[5]. The domain is discretized by 168,564 spectral elements with the element skeleton constructed using the meshing software Cubit [4] in a block-structured way that allows for local grid adaptation (see Fig. 2-a). The number of elements remained constant during the simulation so that for the chosen polynomial order the equation are discretized using 57.8 million unique discretization points, resulting in resolutions of better than 0.1 mm in the radial and axial directions an 0.2 mm in the azimuthal. The distance of the first point from the walls inside the cylinder is 0.06 mm, while in the valve gap the spatial resolution is approximately 0.07 mm. The transient inflow velocity at the intake channel of the upstream plenum is determined by the product of the instantaneous piston speed and the piston-to-valve gap area ratio. Zero velocities are imposed at all stationary walls and the piston speed is set on the moving piston. The ambient pressure and temperature are taken to be uniform at 1 atm and 300 K and the working fluid is air. The simulation is initialized with a zero velocity field with the piston positioned at TDC and 11 consecutive cycles were calculated in total. The simulation was performed on 2496 processors of a Cray XE6 system requiring approximately 160,000 CPU $\times$ h per cycle. Additional details on the numerical approach, resolution requirements and flow dynamics can be found in [27].

3.2 Large Eddy Simulation

LES was performed using the finite volume CFD code OpenFOAM [31], which was extended for this work by the WALE subgrid scale (SGS) model in its compressible formulation [23] and by an improved mesh motion strategy, which is particularly suitable for IC engines [21, 14].

In the eddy-viscosity based WALE model, the subgrid scale stress tensor is defined as:

$$\tau_{ij}^{sgs} = 2\mu_{sgs}\left(\tilde{S}_{ij} - \frac{1}{3}\tilde{S}_{mm}\delta_{ij}\right) - \frac{2}{3}\frac{C_I'}{\bar{\rho}}\frac{\mu_{sgs}^2}{\bar{\Delta}^2}\delta_{ij} \tag{1}$$

where the subgrid viscosity is calculated as

$$\mu_{sgs} = \bar{\rho}\left(C_w\bar{\Delta}\right)^2 \frac{\left(s_{ij}^d s_{ij}^d\right)^{\frac{3}{2}}}{(\tilde{S}_{ij}\tilde{S}_{ij})^{5/2} + \left(s_{ij}^d s_{ij}^d\right)^{5/4}} \tag{2}$$

The above expression (Eq. (2)) can be written in compact form by introducing the operators $\widetilde{OP}_1$ and $\widetilde{OP}_2$

$$\mu_{sgs} = \bar{\rho}\left(C_w\bar{\Delta}\right)^2 \frac{\widetilde{OP}_1}{\widetilde{OP}_2} \tag{3}$$

where:

$$\widetilde{OP}_1 = \left(s_{ij}^d s_{ij}^d\right)^{\frac{3}{2}}$$
$$\widetilde{OP}_2 = (\tilde{S}_{ij}\tilde{S}_{ij})^{5/2} + \left(s_{ij}^d s_{ij}^d\right)^{5/4}$$

which are based on s_{ij}^d, the traceless symmetric part of the square of the velocity gradient tensor $\tilde{g}_{ij} = \partial\tilde{u}_i/\partial x_j$

$$s_{ij}^d = \frac{1}{2}\left(\tilde{g}_{ij}^2 + \tilde{g}_{ji}^2\right) - \frac{1}{3}\delta_{ij}\tilde{g}_{kk}^2 \tag{4}$$

and the resolved rate-of-strain tensor

$$\tilde{S}_{ij} = \frac{1}{2}\left(\frac{\partial\tilde{u}_i}{\partial x_j} + \frac{\partial\tilde{u}_j}{\partial x_i}\right) \tag{5}$$

In the above equations, $\bar{\Delta}$ is the LES filter width (estimated as the cubic root of cell volume), $\bar{\rho}$ is the filtered density whereas the tilde denotes the Favre-filtered quantities [8].

In Eq. (1) a constant value for $C_I' = 45.8$ is used, as suggested in [36]. Since with the WALE model the invariant $\tilde{S}_{ij}\tilde{S}_{ij}$ is zero in the case of pure shear, the model is able to reproduce the laminar to turbulent transition. The formulation of the WALE model is based on the operator $s_{ij}^d s_{ij}^d$ and this represents its main advantage with respect to the dynamic Smagorinsky model, since it is sensitive to both the strain and the rotation rate of the small turbulent structures. Since no explicit filtering is needed and only local information is required to compute the eddy viscosity, the model is well suited for LES in complex geometries with structured or unstructured meshes. In Eq. (2), the ratio $\widetilde{OP}_1/(\tilde{S}_{ij}\tilde{S}_{ij})^{5/2}$ ensures the y^3 behavior of the subgrid viscosity near the wall. At the same time, $\widetilde{OP}_1/(\tilde{S}_{ij}\tilde{S}_{ij})^{5/2}$ is not well conditioned numerically since the denominator can locally tend to zero while $\widetilde{OP}_1$ remains finite. The way used in [17] to avoid this problem is to scale $\widetilde{OP}_1$ by $(\tilde{S}_{ij}\tilde{S}_{ij})^{5/2} + (s_{ij}^d s_{ij}^d)^{5/4}$; the second term in the denominator is negligible near the wall but it avoids numerical instabilities because $\widetilde{OP}_2$ does not go to zero for pure shear or irrotational strain. Although a dynamic procedure could also be applied to the WALE model, in this work C_w was considered as constant, with a value of 0.3, assessed from the case of isotropic homogeneous turbulence [17].

The mesh motion strategy employed in the simulations is based on a point-stretching concept. Given $\mathbf{U}_{\text{piston}}$ as the piston velocity ($\mathbf{U}_{\text{piston}} = S/2\sin(\omega t)\mathbf{i}_c$; where S is the piston stroke and $\mathbf{i}_c$ the unit vector in the direction of the cylinder axis), the velocity $\mathbf{u}_p$ at a point $\mathbf{x}_p = (x_p, y_p, z_p)$ is calculated as:

$$\mathbf{u}_p(\mathbf{x}_p) = \mathbf{U}_{\text{piston}} \cdot \frac{z_{\max} - z_p}{z_{\max} - z_{\text{piston}}} \tag{6}$$

where $z_{\max}$ and z_{piston} are the z-coordinates delimiting the moving cell region:

$$z_{\max} = -c \tag{7}$$

$$z_{\text{piston}} = -\left[c + S/2(1-\cos\theta)\right] \tag{8}$$

c and S are, respectively, the clearance height and the stroke (see Fig. 1) and θ the crank-angle; z_p is the z-coordinate of the generic mesh point p. The velocity $\mathbf{u}_p$ of Eq. (6) enters into the conservation equation through the mesh-motion cell face flux that is subtracted from the advective cell face flux to ensure mass conservation.

The domain is discretized by a purely hexahedral mesh with about 4.6 million elements (Fig. 2-b). The resulting cell size in the cylinder region is 0.2 mm in the radial direction and 0.25 in the axial one. The azimuthal cell size ranges from approximately 1.5 mm on the external circumference and 0.18 mm near the cylinder axis. The innermost part of the cylinder was discretized using an O-grid type mesh to avoid low-quality cells in proximity of the valve axis. In the valve seat the near-wall resolution is about 0.07 mm.

The filtered Navier-Stokes equations were solved using a Finite Volume (FV) solver based on the transient-SIMPLE algorithm [34]. This choice was driven by the necessity to ensure convergence of the pressure-velocity coupling at each timestep without being limited by the Courant-Friedrichs-Lewy (CFL) criterion, as it would happen if the classical PISO procedure were employed. Temporal integration was performed with a fixed angular step equal to $\Delta\theta = 0.05°$; as a consequence, the maximum Courant number ranged from 0.75 (near bottom- and top-dead-center) to approximately 11 around $\theta = 90° + k\,180°$, with $k = \left[0; N_{\text{cycles}}\right]$. A second-order backward differencing scheme was used to discretize the time derivatives, whereas momentum convection is performed with the Linear-Upwind Stabilized Transport (LUST) scheme, a low-dissipation method specifically developed for LES [35]. For the remaining differential terms, pure second-order differencing schemes were used, with the exception of the energy equation, for which an upwind-biased method was employed for stability.

3.3 Averaging

In stationary flows, statistical quantities are usually computed by averaging in time. For non-stationary flows in time-varying geometries, ensemble-averaging should be used instead. This results in significantly higher computational cost since a sufficient number of cycles must be simulated in order to obtain converged statistics. Taking advantage of the axisymmetric geometry considered here, a combination of azimuthal and ensemble averaging, referred to henceforth as total averaging, is exploited to reduce the number of required cycles. In total, eight engine cycles (by DNS) and ten (by LES) were simulated; the first two cycles were discarded from the statistical analysis, in order to minimize the effect of the initial conditions. A similar algorithm for averaging was used by Liu and Haworth [11], who simulated five cycles of the same engine. The convergence of the statistics can be assessed by looking at the value of the tangential component of velocity U_ϕ, which is expected to be zero in the averaged quantities, because of the axis-symmetric geometry. Results are shown in Fig. 3, where the instantaneous velocity U_ϕ is compared against the spatial average and the total average. Convergence is achieved almost everywhere both for LES and DNS. Only in DNS simulation (Fig. 3-a) there is a small region near the cylinder axis ($r/R_c = 0$) in which the average has not converged: the possible reason is that the number of data points needed for a statistical convergence in this area would have been too high for the adopted grid resolution.

(a) DNS (nek5000) (b) LES (OpenFOAM)

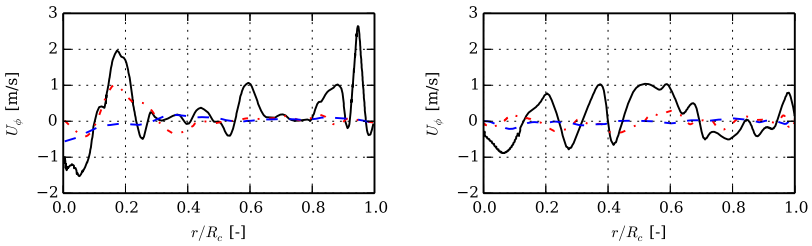

Fig. 3 Radial distribution of azimuthal velocity U_ϕ at CA = 90°, z = -22.5 mm for the third engine cycle. — instantaneous velocity; — · — spatial average; - - - spatial and ensemble average. (a) NEK5000, (b) OpenFOAM

4 Results

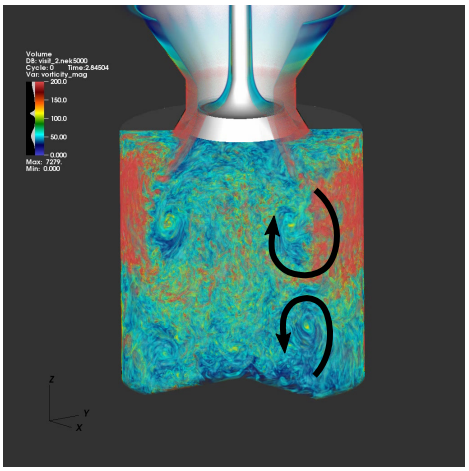

Fig. 4 Volume rendering of the instantaneous DNS vorticity magnitude at 125° CA of the first cycle [15].

Starting from a quiescent velocity field, eight (DNS) and ten (LES) cycles were simulated in total. A complex flow field consisting of interacting large-scale coherent structures and a large number of smaller vortices is obtained as can be seen in Fig. 4. The flow fields were found to vary substantially from cycle to cycle, with the velocity at the top dead center (TDC) of one cycle strongly affecting the hollow jet at the valve exit and the flow field evolution of the subsequent cycle. The flow dynamics are dominated by three vortex rings formed during the downward piston motion in the central part below the valve, the corners between the liner and the cylinder head at the beginning of the cycle, and between the liner and the piston after approximately 90° CA. A multitude of smaller vortices are generated mainly at the shear layers of time-varying momentum at both sides of the hollow jet, and by the impingement of the jet onto the cylinder liner. The momentum, stability and orien-

tation of the central vortex ring relative to the axis effectively determines the flow field at top dead center [29]. When the jet center is sufficiently displaced from the cylinder axis, the central vortex ring becomes tilted and is only partially pushed through the valve during the compression stroke, leaving large coherent structures at TDC, which create an asymmetric flow in the radial direction. Otherwise, an almost horizontal vortex ring is formed around the axis, which is convected to the plenum through the open valve leaving only the axisymmetric vortex at the piston/liner corner at TDC. The radial velocity at TDC affects strongly the flow dynamics of the subsequent cycle and results in the observed cyclic variations [29]. The aforementioned phenomena drastically change if the valve is closed during piston upward stroke. In this case density variation become relevant and the incompressible approximation does not hold anymore. Follow up DNS which investigated the effect of compression on the flow, temperature and composition fields in the closed cylinder [28] revealed significant changes mainly due to the reduction of the kinematic viscosity and turbulent convective heat transfer from the walls towards the inner part of the cylinder.

4.1 Averaged fields

The simulated cycles have been post-processed to calculate the ensemble- and azimuthally-averaged (total) means and fluctuations of the velocity. Streamlines of the mean velocity field extracted from the experiments [16] have been compared with the numerical ones in Fig. 5 at 36°, 90°, 144° and 270° CA (first to fourth row, respectively). DNS results are in very good agreement with the available experimental data at all times and locations. At 36° CA the jet enters the cylinder forming two recirculation zones at either side of jet. The position and direction of the incoming jet, the position and sizes of the recirculation zones and the axial position of the broadening of the jet streamlines of the LES agrees well with the DNS and experimental results. At 90° CA, where the piston speed reaches its maximum, the DNS and the experiment show a large central vortex ring in the cylinder center and two secondary rings at the edges between liner and piston cylinder head. The general structure is well predicted by LES, but the large central vortex ring appears larger. As a result, the secondary vortex ring between liner and piston nearly vanished. The agreement of the LES strongly improves at 144° CA. The location and the spatial extent of the three vortex rings is well predicted, indicating that the LES can capture the mean field close to BDC.

During the exhaust stroke, the mean flow becomes essentially one-dimensional as it can already be seen at 270° CA (last row of Fig. 5). Experiments and DNS show a slight bend of the streamlines near the piston head, which is due to the vortex rings formed during the intake stroke; this bend was been found to play an important role for the jet trajectory of the following cycle.

Mean and RMS fluctuations of the axial velocity have been compared in Fig. 6 at selected axial distances z below the cylinder head. At 36° CA the flow is mainly drawn in the axial direction and the jet velocity is respectively almost ten and five times the mean piston speed U_{piston} at $z = 10$ and 20 mm below the cylinder head; the radial location of the maximum values remain unaffected by the distance from the cylinder head. In the vicinity of the piston the mean profile is almost uniform and flow velocity is mainly determined by U_{piston}. The rms velocity profiles show that turbulence is generated in the shear layers between the incoming jet and the fluid inside the cylinder. As indicated by the streamlines, the LES results agree well with the experimental and DNS results. This is also true for the rms velocities at 36° CA, which predict the magnitude very well but are slightly shifted towards the cylinder wall.

Following jet deflection at approximately 90° CA, the peak values of the velocity shift towards the cylinder wall, before the axial profiles flatten for $z < 40$ mm. The differences in the rms values of the LES simulation at 90° CA and $20 \leq z \leq 40$ result from the differences in the mean flow, as can also be seen in the streamline plot (Fig. 5). At 144° CA the mean and rms velocities are well predicted by both approaches. The LES results are in good agreement with the experimental and DNS data at 36° CA and 144° CA. However, at 90° CA the axial velocities at the cylinder wall is overpredicted. This can be due to the different reasons: first, the flow field at 90° CA is sensitive to the jet breakup process which renders the jet flow turbulent and is not easy to capture by LES. In addition, as shown in [27], the DNS shows that at 90° CA the strong shear stresses result in small integral length scales in the shear layers of the incoming jet, indicating that higher resolution should be used in LES in order to resolve the steep gradients.

The Length Scale Resolution parameter (LSR) has been used for estimating the LES completeness [3]. According to Pope [25], an LES is considered to be complete if it resolves at least 80% of the kinetic energy contained in the flow. Though the completeness can be in principle assessed by directly computing the ratio between resolved and unresolved (i.e. subgrid) kinetic energy, this is seldom done since it does not provide information about the adequacy of local mesh resolution. LSR instead compares the local filter width with the lower limit of the inertial subrange:

$$\mathrm{LSR} = \frac{\bar{\Delta}}{\ell_{DI}}, \quad \ell_{DI} = 60\eta \tag{9}$$

where η is the Kolmogorov length scale, estimated as:

$$\eta = \nu^{3/4}\varepsilon^{-1/4} \tag{10}$$

with ε being the turbulent kinetic energy dissipation:

$$\varepsilon = C_\varepsilon \frac{k_{sgs}^{3/2}}{\bar{\Delta}}, \quad C_\varepsilon = 1.048 \tag{11}$$

where k_{sgs} is the subgrid kinetic energy and $\bar{\Delta}$ the local filter width. It was found that LSR provides a more precise estimation of the local grid resolution and may provide hints about the overall simulation quality [23, 22]. Experience showed that $\mathrm{LSR} \leq 5$ can be used as a quality threshold to assess local mesh resolution.

In Fig. 7 the contour plots of LSR at six representative crank angles of the third cycle are depicted. At TDC and at 36° CA (Figs. 7-a and 7-b respectively) velocities are very low and LSR is well below the threshold everywhere, and the resolution is enough for resolving all scales down to the dissipation range. With increasing crank angles, until BDC is reached, the LSR grows as an outcome of two effects: the increasing velocity of the jet stream and the increasing size of the cells in the cylinder due to the mesh motion. At 90° CA (Fig. 7-c) and 144° (Fig. 7-d) there are regions where the LSR values are quite high and the threshold value is exceeded, particularly where the jet breaks up and impinges against the liner walls, indicating that the smallest resolved length scale is too far from the lower bound of the inertial subrange; consequently, the energy transfer from large to small scales is not correctly accounted and discrepancies in both the mean velocity and rms fluctuations can be observed.

4.2 Cycle-to-Cycle Variability

Cycle-to-cycle variability was estimated using the volume-averaged velocity magnitude $|U|(t)$, defined in Eq. (12).

$$|U|(t) = \frac{1}{(V+V_c)} \int_{(V+V_c)} U(\mathbf{x},t)\, \mathrm{d}V \tag{12}$$

Volume averaging was limited to the cylinder region to exclude any influence of the upper plenum that could mask the variability. The normalized value of $|U|$ is reported against crank-angle in Fig. 8. The cycle-to-cycle variations are apparent at the local maxima and the peak values of the kinetic energy follow a non-monotonic variation.

The sequence of cycles having a high peak values with cycles having low peak values of kinetic energy is an indicator of an existing periodic cycle-to-cycle variability; at the same time, the limited number of computed cycles does not allow for more concrete conclusions. Compared to DNS, LES shows increased maximum and decreased minimum values of the kinetic energy and, therefore, a different prediction of the dissipation. This is also apparent in Fig. 8-b, where the integrated values of $|U|$ are plotted against the relative crank angle during the expansion stroke: the jet trajectory and the jet-wall interaction are strongly related to the dissipation rate. Maximum values of the peak of kinetic energy calculated by LES are higher than the corresponding values achieved by DNS; also a time shift of 20° in their location is present. Fig. 9-a, showing the phase-averaged values of $|U|$, confirms this behavior.

A measure of the CCV is achieved by looking at the normalized standard deviation of $|U|$ plotted in Fig. 9-b. If the first part of the intake stroke (up to 20° CA, where the flow is dominated by the laminar vortex ring) is neglected by the analysis, DNS shows the maximum deviation at about 100° CA, in correspondence to the maximum values of $|U|$; in LES, the maximum is about at 60° CA, probably because the lower dissipation in the computed flow causes a higher variability in the local flow, when the interaction between the incoming ring jet and the surrounding field is stronger.

The evolving flow features are shown in Figs. 10, 11 and 12, where vorticity contours at 36°, 58.75° and 76.5° during the expansion stroke are printed. At CA = 36° the laminar jet that enters into the cylinder interacts with a strong turbulent field that determines its evolution during the following stages. In fact, during the third cycle, when the overall turbulence level is lower, the vortex formed at the end of the jet is large and almost symmetric; at cycle no. 6, that is characterized by a higher turbulence level, the primary vortex ring is narrow and it is strongly disturbed by the turbulent fluctuations around it (Fig. 10). Moreover, the breakup of the annular jet occurs closer to the cylinder head and the Kelvin-Helmoltz instability observed on the sides of the jet starts growing earlier with respect to the third cycle (Fig. 11). The different breakup of the laminar jet yields to completely different flow structures near the piston wall. During the third cycle a counter-rotating secondary vortex ring is generated between the main jet and the piston, as apparent both by DNS and LES (Fig. 11). During cycle no. 6, on the other hand, the incoming jet impinges onto the liner walls and a single larger vortex is generated, that occupies nearly the entire cylinder region. The same structures persists for some degrees and can be seen also in Fig. 12 which shows the instantaneous vorticity field at 76.5° CA. With respect to the evolution of turbulence-generated structures, both approaches show their ability to predict the flow dynamics. Even though the turbulent intensity computed by LES is somewhat less accurate, the fundamental mechanics of turbulence can be simulated with a good degree of predictability, at least in a qualitative sense.

4.3 POD analysis

The LES results were further analyzed using phase-dependent Proper Orthogonal Decomposition (POD). POD consists in decomposing a time-varying velocity field $\mathbf{u}(\mathbf{x},t)$ into M independent pairs $[a^{(k)}(t), \psi^{(k)}(\mathbf{x})]$, where $a^{(k)}(t)$ is a time-dependent coefficient expressing the energy content of the *k-th* mode, and $\psi^{(k)}(\mathbf{x})$ is the corresponding spatial basis function:

$$\mathbf{u}(\mathbf{x},t) = \sum_{k=1}^{M} \left[a^{(k)}(t)\psi^{(k)}(\mathbf{x}) \right] \tag{13}$$

POD modes are usually extracted by the so-called "method of snapshots", originally developed by Sirovich [30], to reduce the computational cost of formal methods [2]. The number of modes that can be computed from a field equals the number of time realizations (snapshots) that enter the POD calculation. By convention, eigenvalues and eigenvectors of the data covariance matrix are ordered by decreasing magnitude of the eigenvalues, so that the energy content of POD modes $[\psi^{(1)} \dots \psi^{(M)}]$ will be in decreasing order as well. Since a reciprocating engine is characterized by a periodic operation due to its varying geometry, it is generally not appropriate to consider the temporal index i as $\theta = i\,\Delta\theta$ (being $\Delta\theta$ the integration step). One solution is to calculate a "phase-dependent" POD: for each crank-angle position a different POD is calculated, where the number of snapshots is defined by the total number of simulated engine cycles. It is worth mentioning that an alternative method is available, namely the "phase-independent" POD, where linear transformations are applied to the FV grid and to the velocity field for each crank-angle; the total number of realizations equals the number of saved timesteps. The "phase independent" POD has been developed by Fogleman *et al.* [7] and applied to LES results of the present valve-piston assembly by Liu and Haworth [12]. However, in the current paper, the former approach has been chosen because, in authors' opinion, it allows for a better physical insight of the dynamics of turbulence of in-cylinder flows.

In the method of snapshots, the number of modes that can be extracted equals the number of computed fields; for a phase-dependent POD this is equal to the number of simulated cycles. In Fig. 13, the first four eigenvalues are plotted against crank-angle degrees, providing information about the energy content of each mode at different piston positions. The eigenvectors of the POD modes provide an alternative way to decompose the flow field and the dominant first mode strongly resembles the mean velocity plot. Their contours at 90° CA and 144° CA are presented in Figs. 14-a and 14-b, respectively.

For the purposes of this section, only the first four modes are presented out of the total of ten. In Figs. 13-a, 13-c and 13-e, the eigenvalues of each mode are presented for each velocity component U_x, U_y, and U_z, respectively. Figs. 13-b, 13-d and 13-f report the ratio $r_{i,i+1} = a_i/a_{i+1}$ of consecutive eigenvalues. This parameter can be regarded as an indicator of the level of organization of the flow: when $r_{i,i+1}$ is high, most of the kinetic energy is contained in the first modes, whereas the remaining modes are less energetic. Conversely, when $r_{i,i+1} \approx 1$ the energy is uniformly distributed between modes. The trend of the curves of the first mode in Figs. 13-a and 13-c reflects the variation of the piston velocity. As it can be observed, the curves have absolute minima at dead centers and local maxima around the middle of the expansion and the compression stroke. The POD data for the second velocity component u_y are not shown: they are almost identical to those of u_x, because of the axisymmetric geometry. In all the graphs, the ratio $r_{1,2}$ between the first and the second eigenvalue is always significant, ranging from a minimum value of 2 (e.g. at dead centers for x-component) to a maximum of 100 (approximately at 270° CA for the z-component).

The ratio between eigenvalues of greater order is much smaller, being always limited in a range between 1 and 2. The unorganized character of the flow near the top and bottom dead centers is evidenced by the low values of $r_{1,2}$ in Fig. 13. However, since the flow is pushed into the reservoir and a strong upward jet generates, the value of $r_{1,2}$ related to u_z remains high.

As the piston accelerates, a hollow jet is formed under the valve and the level of coherent structures increases, especially with respect to u_x and u_y. At 90° CA the eigenvalue ratios are higher, not only between the first two modes, but also among successive ones. In the contour plots of Fig. 14-a the flow structures can be clearly recognized. The first mode has a strong resemblance to the mean flow field, while the second mode reveals smaller structures, that are reminiscent of the turbulence cascade from large to small eddies. At 144° CA, which corresponds to the maximum degree of CCV, the first POD mode is still quite energetic, and its contour plot (Fig. 14-b) has a strong affinity with the mean velocity field. However, the second mode has a smaller eddy length scale, with most of the energy concentrated in the jet shear layer. It must be noted, however, that the averaged flow field is the outcome of a operation of reduction and some information about the turbulence dynamics are inevitably lost. This is particularly apparent when the first two POD modes are compared with the average flow fields at 90° CA (Fig.14-a). The averaged flow field shows a main vortex ring with higher velocity values, but no hint of the secondary vortex, which is not generated at each cycle, is observed in Figs. 11 and 12. On the other hand, the primary vortex ring is clearly recognizable in the first POD mode at 90° CA (Fig. 14-a), since it contains the largest part of kinetic energy, but a hint of the secondary vortex can be seen in the second POD mode at 90°; this secondary vortex is, however, not visible in the average velocity contour. At 144° CA secondary structures do not have sufficient energy to appear clearly in the eigenvector plot of the second mode, but the contours of Fig. 14-b can give an approximate idea of their lengthscale. Finally, during the compression stroke, most turbulent features are advected into the plenum or dissipated by the upward motion of the piston. Thus, as one might expect, the contour plots of velocity modes (not shown here for brevity) represent only small scales which have almost the same energy level.

5 Conclusions

Direct and large eddy simulation methodologies were employed to study numerically the unsteady flow inside a time varying engine-like geometry. DNS was performed by a ALE-based spectral element code to account for the moving grid, while LES was carried out with a finite volume solver on a purely hexahedral mesh. Comparisons of numerical results obtained by both techniques with the available experimental data showed that DNS predicted with very good accuracy the average and RMS velocities for all crank angles and positions, whereas LES shows larger differences with respect to the measured flow field for crank angles around 90° CA. Both methods were used to investigate cycle-to-cycle variability due to turbulence-related phenomena. CCV was measured using the in-cylinder average velocity as an indicator. Similar results were obtained both by DNS and LES, even though some differences persisted in relation to the crank-angle position and the amount of CCV during the intake stroke. Differences may be due to the increased resolution requirements around 90° CA when the piston speed attains its maximum value and the sensitivity of the jet breakup process.

The same evolving turbulent structures were properly reproduced and, for the limited number of cycles simulated, a periodic trend of CCV was observed by both methods. The use

of a C_w value for the LES model extracted from the DNS data for the geometry considered here or the adoption of a dynamic procedure may result in better agreement and will be investigated in a future study.

Finally, the LES results were analyzed with POD to gain a deeper insight into the flow dynamics. POD is demonstrated to be able to detect dynamic turbulent structures that can be observed by a time-resolved flow visualization but are averaged out by a classical statistical analysis. In this sense, phase-dependent POD can provide information not only on the global level of organization of the flow, but also on the turbulence dynamics therein involved.

Acknowledgements The DNS work was performed within project 200021_135514 funded by the Swiss National Science Foundation (SNF) on the computational resources of the Swiss Super Computing Center (CSCS) under project number s189.

References

1. Amsden, A., O'Rourke, P., Butler, T.: KIVA-II: A Computer Program for Chemically Reactive Flows with Sprays. LA 11560-MS, Los Alamos National Laboratory (1989)
2. Berkooz, G., Holmes, P., Lumley, J.L.: The proper orthogonal decomposition in the analysis of turbulent flows. Annual Review of Fluid Mechanics **25**(16), 539–575 (1993)
3. Brusiani, F., Forte, C., Bianchi, G.: Assessment of a Numerical Methodology for Large Eddy Simulation of ICE Wall Bounded Non-Reactive Flows. In: SAE Technical Paper 2007-01-4145 (2007). DOI doi:10.4271/2007-01-4145
4. Cubit: Cubit (2012). Sandia National Laboratories, Meshing Software
5. Deville, M., Fischer, P., Mund, E.: High-order methods for incompressible fluid flow. Cambridge University Press, New-York (2002)
6. Fischer, P.F., Lottes, J.W., Kerkemeier, S.G.: nek5000 web page (2008). http://nek5000.mcs.anl.gov
7. Fogleman, A.A., Lumley, K., Rempfer, D., Haworth, D.C.: Application of the proper orthogonal decomposition to datasets of internal combustion engine flows. Journal of Turbulence **5**(23), 1–18 (2004)
8. Garnier, E., Nikolaus, A., Sagaut, P.: Large Eddy Simulation for Compressible Flows, 2009 edn. Springer (2009)
9. Hasse, C., Sohm, V., Durst, B.: Numerical investigation of cyclic variations in gasoline engines using a hybrid URANS/LES modeling approach. Computers & Fluids **39**(1), 25–48 (2010). DOI 10.1016/j.compfluid.2009.07.001
10. Haworth, D.C., Jansen, K.: Large-eddy simulation on unstructured deforming meshes: towards reciprocating IC engines. Computers & Fluids **29**, 493–524 (2000)
11. Liu, K., Haworth, D.C.: Large-eddy simulation for an axisymmetric piston-cylinder assembly with and without swirl. Flow, Turbulence and Combustion **85**, 297–307 (2010). DOI 10.1007/s10494-010-9292-1
12. Liu, K., Haworth, D.C.: Development and assessment of POD for analysis of turbulent flow in piston engines. SAE technical paper 2011-01-0830 (2011)
13. Montorfano, A., Piscaglia, F., Ferrari, G.: Inlet Boundary Conditions for Incompressible LES: a Comparative Study. Mathematical and Computer Modelling (2011). Doi:10.1016/j.mcm.2011.10.077
14. Montorfano, A., Piscaglia, F., Onorati, A.: An extension of the dynamic mesh handling with topological changes for LES of ICE in OpenFOAM. SAE World Congress & Exhibition 2015, paper n. 2015-01-0384 (2015)
15. Montorfano, A., Piscaglia, F., Onorati, A.: A LES Study on the Evolution of Turbulent Structures in Moving Engine Geometries by an Open-Source CFD Code. SAE World Congress & Exhibition 2014, paper n. 2014-01-1147 (2014)
16. Morse, A.P., Whitelaw, J.H., Yanneskis, M.: Turbulent flow measurements by laser-doppler anemometry in motored piston-cylinder assemblies. Journal of Fluids Engineering **101**, 208–216 (1979)
17. Nicoud, F., Ducros, F.: Subgrid-scale stress modelling based on the square of the velocity gradient tensor. Flow, Turbulence and Combustion **62**, 183–200 (1999). DOI 10.1023/A:1009995426001
18. Piscaglia, F., Montorfano, A., Onorati, A.: A scale adaptive filtering technique for turbulence modeling of unsteady flows in IC engines. SAE Int. J. Engines **8**(2):426-436, 2015, doi:10.4271/2015-01-0395.
19. Piscaglia, F., Montorfano, A., Onorati, A.: Improving the Simulation of the Acoustic Performance of Complex Silencers for ICE by a Multi-Dimensional Non-Linear Approach. SAE Int. J. Engines **2**(5), 633–648 (2012). Doi:10.4271/2012-01-0828

20. Piscaglia, F., Montorfano, A., Onorati, A.: Development of a Non-Reflecting Boundary Condition for Multidimensional Nonlinear Duct Acoustic Computation. Journal of Sound and Vibration **332**(4), 922–935 (2013). DOI http://dx.doi.org/10.1016/j.jsv.2012.09.030.
21. Piscaglia, F., Montorfano, A., Onorati, A.: Development of Fully-Automatic Parallel Algorithms for Mesh Handling in the OpenFOAM-2.2.x Technology. SAE Technical Paper 2013-24-0027 (2013). DOI doi:10.4271/2013-24-0027
22. Piscaglia, F., Montorfano, A., Onorati, A.: Towards the LES Simulation of IC Engines with Parallel Topologically Changing Meshes. SAE Int. J. Engines, **6**(2), 926–940 (2013). DOI 10.4271/2013-01-1096
23. Piscaglia, F., Montorfano, A., Onorati, A., Brusiani, F.: Boundary conditions and sgs models for les of wall-bounded separated flows: An application to engine-like geometries. Oil Gas Sci. Technol. - Rev. IFP Energies nouvelles **69**(1), 11–27 (2014). DOI 10.2516/ogst/2013143. URL http://dx.doi.org/10.2516/ogst/2013143
24. Pope, S.: Turbulent flows. Cambridge University Press (2000)
25. Pope, S.: Ten questions concerning the large eddy simulation. New journal of Physics **6**, 35 (2004)
26. Sagaut, P.: Large eddy simulation for incompressible flows: an introduction. Scientific computation. Springer-Verlag (2006)
27. Schmitt, M., Frouzakis, C., Tomboulides, A., Wright, Y., Boulouchos, K.: Direct numerical simulation of multiple cycles in a valve/piston assembly. Physics of Fluids **26**(3) (2014)
28. Schmitt, M., Frouzakis, C., Tomboulides, A., Wright, Y., Boulouchos, K.: Direct numerical simulation of the effect of compression on the flow, temperature and composition under engine-like conditions. Proceedings of the Combustion Institute **35(3)**, 3069–3077 (2015)
29. Schmitt, M., Frouzakis, C., Wright, Y., Tomboulides, A., Boulouchos, K.: Investigation of cycle-to-cycle variations in an engine-like geometry. Physics of Fluids **26**(12), 125104 (2014)
30. Sirovich, L.: Turbulence and the dynamic of coherent structures. Quarterly of Applied Mathematics **45**, 561–590 (1987)
31. The OpenFOAM Foundation: OpenFOAM web page (2006). http://www.openfoam.org
32. Thobois, L., Rymer, G., Soulères, T., Poinsot, T.: Large-eddy simulation in IC engine geometries. Sae Paper n. 2004-01-1854, SAE world Congress & exhibition (2004)
33. Thobois, L., Rymer, G., Soulères, T., Poinsot, T., den Heuvel B., V.: Large-eddy simulation for the prediction of aerodynamics in ic engines. In: Int. J. Vehicle Design "New strategies in Automotive Diesel Engines for Meeting Upcoming Pollutant Emission Restrictions" (2005)
34. Versteeg, H.K., Malalasekera, W.: An Introduction to Computational Fluid Dynamics. Prentice Hall College Div, 2nd edition (2007)
35. Weller, H.: Controlling the computational modes of the arbitrarily structured C grid. Monthly Weather Review **140**, 3220–3234 (2012). DOI http://dx.doi.org/10.1175/MWR-D-11-00221.1. URL http://journals.ametsoc.org/doi/pdf/10.1175/MWR-D-11-00221.1
36. Wollblad, C., Davidson, L., Eriksson, L.E.: Large eddy simulation of transonic flow with shock wave/turbulent boundary layer interaction. AIAA Journal **44**, 2340–2353 (2006)

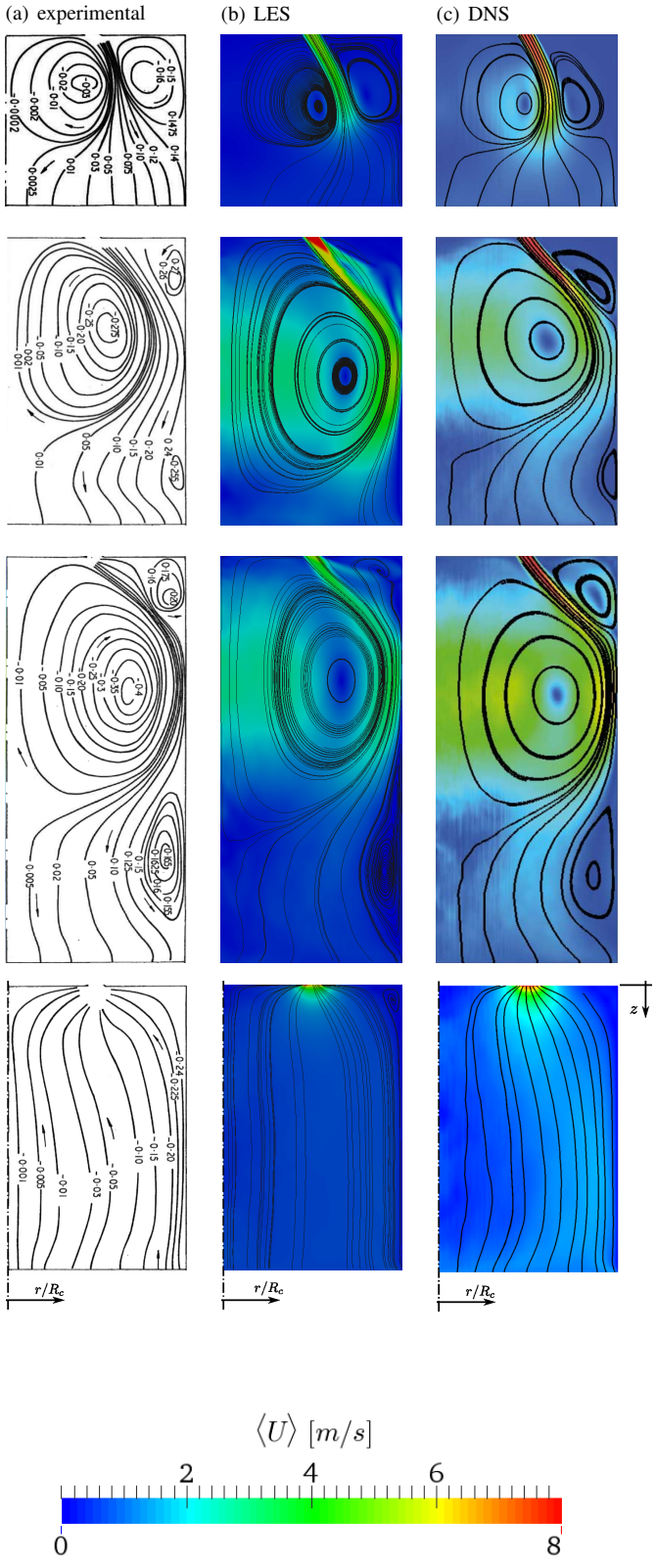

Fig. 5 Comparison of streamlines extracted from the (a) experimental, (b) LES and (c) DNS results at 36° CA (first row), 90° CA (second row), 144° CA (third row) and 270° CA (fourth row). The numerical results are superimposed on contour plots of the mean velocity fields.

(a) 36° CA, $z = -10$ mm

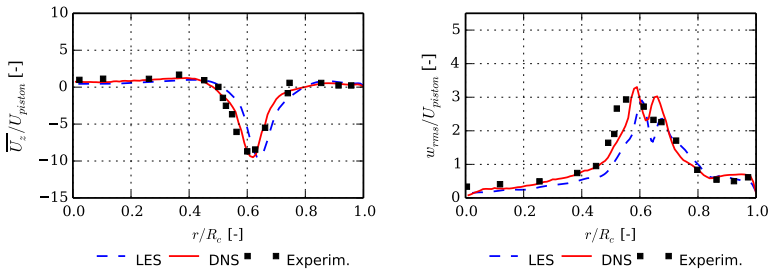

(b) 36° CA, $z = -20$ mm

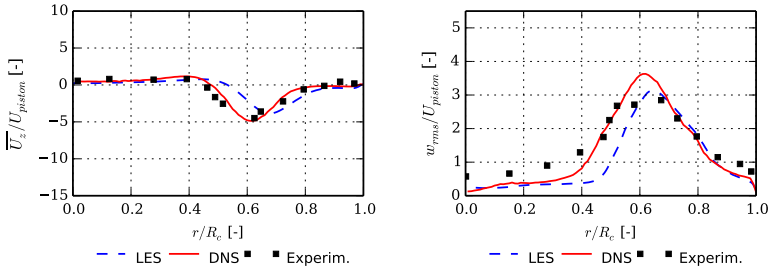

(c) 90° CA, $z = -20$ mm

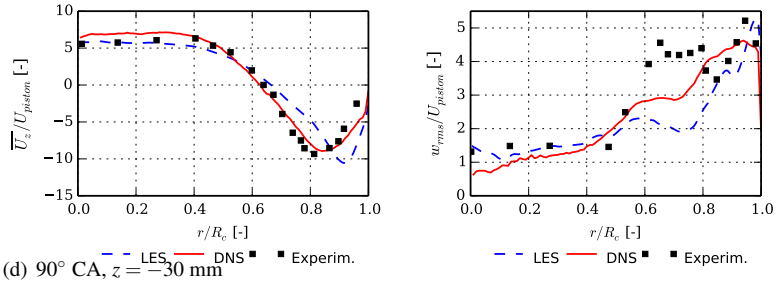

(d) 90° CA, $z = -30$ mm

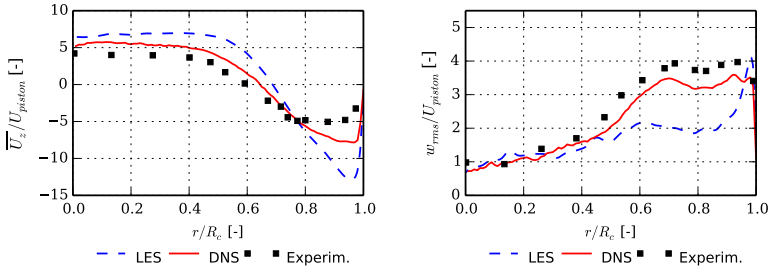

(e) 144° CA, $z = -20$ mm

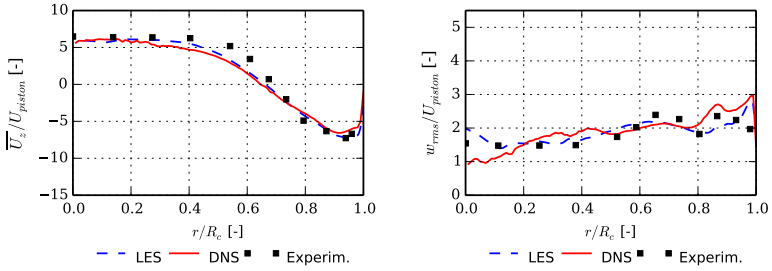

(f) 144° CA, $z = -30$ mm

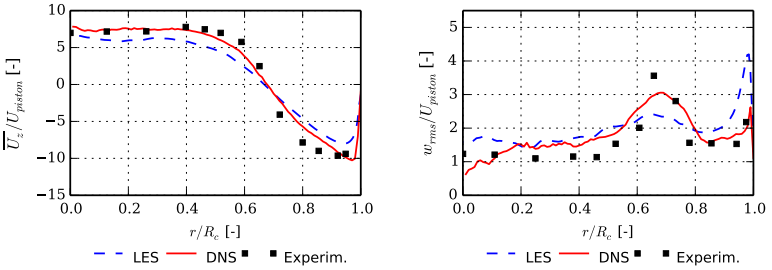

Fig. 6 Comparison of mean axial velocity and RMS fluctuations at selected CA degrees and axial locations.

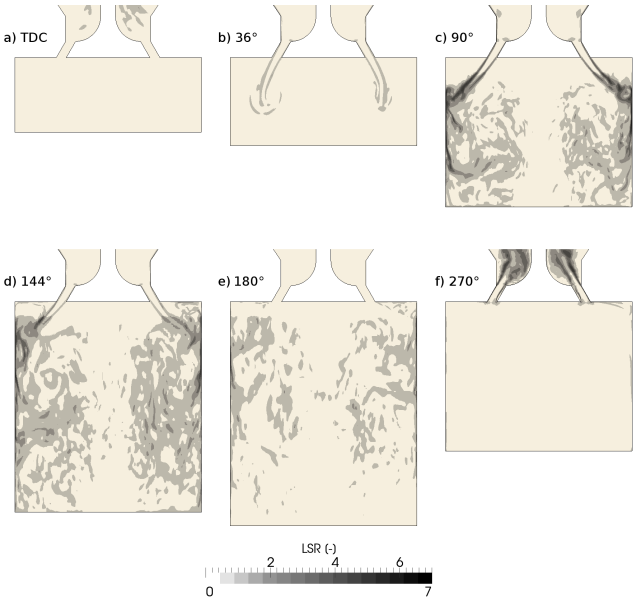

Fig. 7 LSR parameter for six representative crank-angles computed from the LES results. Snapshots are taken from the third engine cycle.

(a) (b)

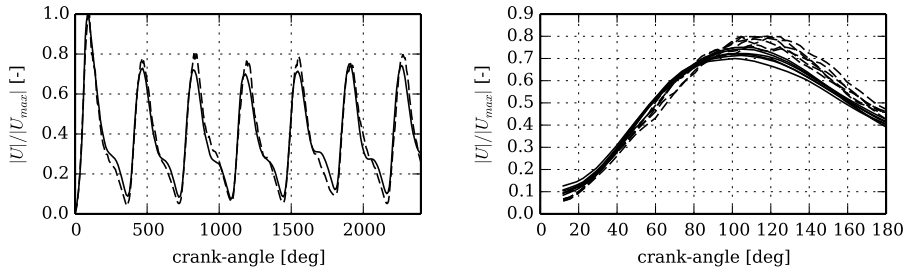

Fig. 8 Comparison of volume-averaged velocity magnitude extracted from the DNS (—) and LES (– –) data. (a) Global view over seven cycles; (b) Trend over the induction stroke for cycles 2-7.

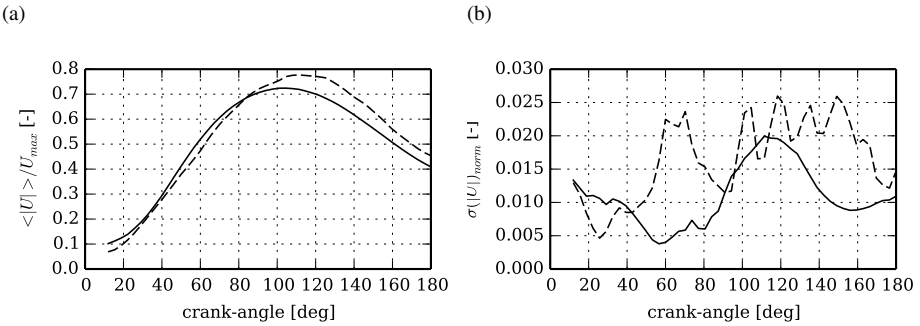

Fig. 9 Comparison of volume-averaged velocity magnitude extracted from the DNS (—) and LES (– –) data. (a) Average values along the expansion stroke. (b) Normalized standard deviation

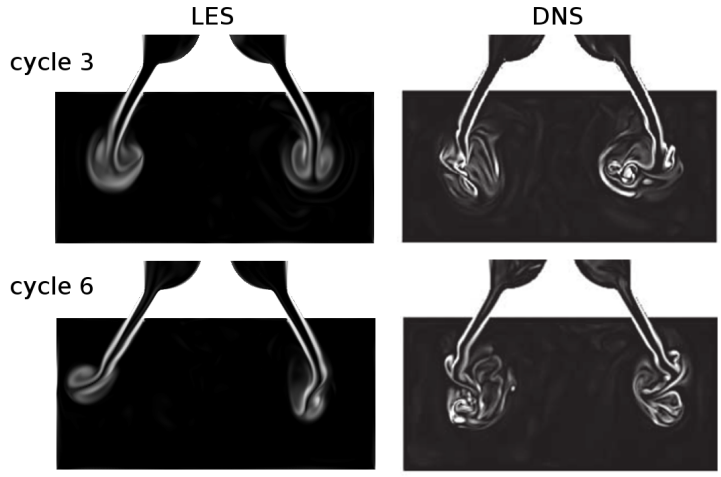

Fig. 10 Snapshot of instantaneous vorticity magnitude on an axial plane at CA = 36° for two different engine cycles.

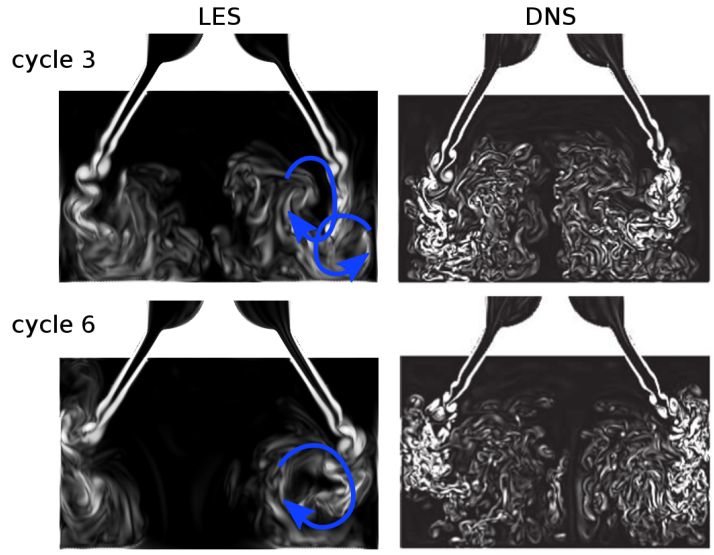

Fig. 11 Snapshot of instantaneous vorticity magnitude on an axial plane at CA = 58.5° for two different engine cycles.

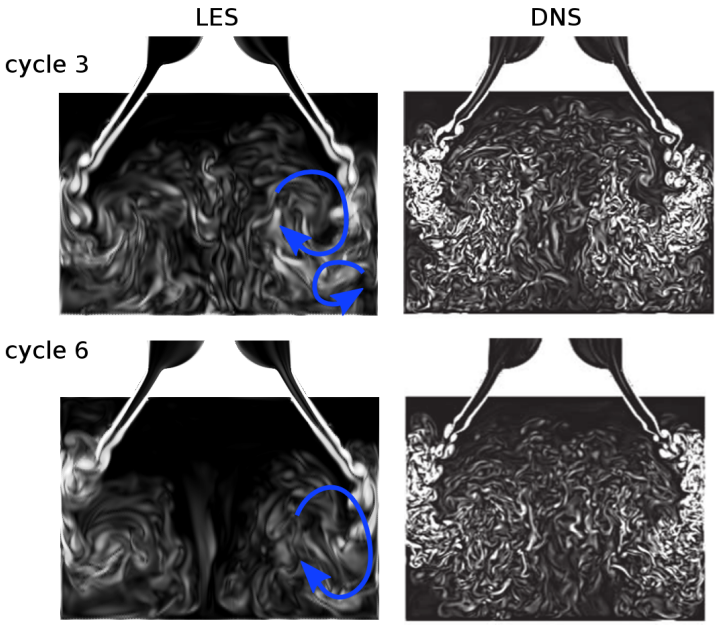

Fig. 12 Snapshot of instantaneous vorticity magnitude on an axial plane at CA = 76.5° for two different engine cycles.

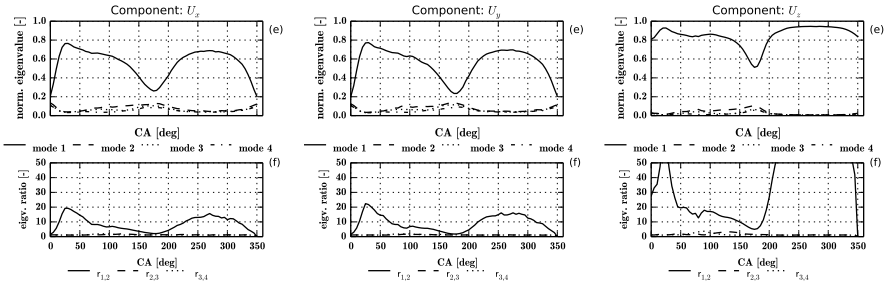

Fig. 13 (a), (c), and (e) Eigenvalues of POD modes versus crank angle for velocity component U_x, U_y and U_z respectively. (b), (d), and (f) Ratios $r_{i,i+1}$ between subsequent eigenvalues for velocity component U_x, U_y, and U_z respectively.

(a) 90° CA

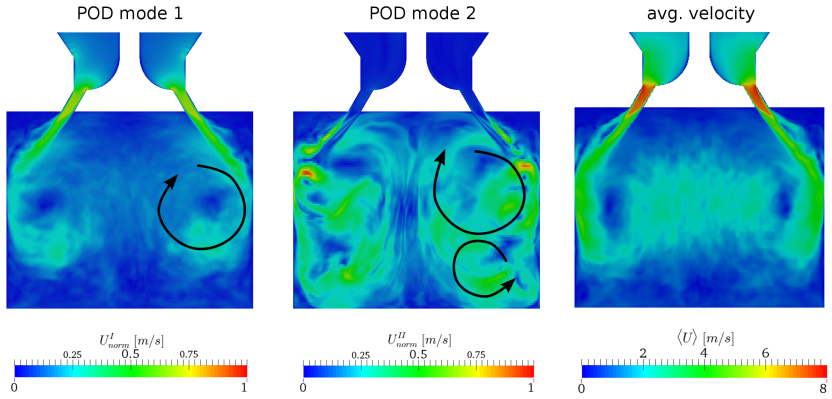

(b) 144° CA

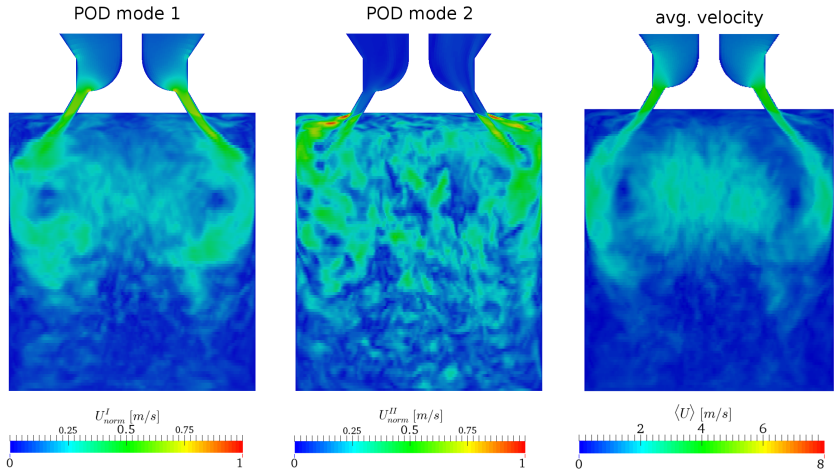

Fig. 14 Eigenvectors of the first two POD modes (normalized values) together with the ensemble-averaged velocity at (a) 90° CA and (b) 144° CA.